Statistical Based Impulsive Noise Removal in Digital Radiography

I. Frosio, *Member, IEEE*, and N. A. Borghese*, *Member, IEEE*

***Abstract*—A new filter to restore radiographic images corrupted by impulsive noise is proposed. It is based on a switching scheme where all the pulses are first detected and then corrected through a median filter. The pulse detector is based on the hypothesis that the major contribution to image noise is given by the photon counting process, with some pixels corrupted by impulsive noise. Such statistics is described by an adequate mixture model. The filter is also able to reliably estimate the sensor gain. Its operation has been verified on both synthetic and real images; the experimental results demonstrate the superiority of the proposed approach in comparison with more traditional methods.**

***Index Terms*—Digital radiography, impulsive noise, mixture models, Poisson noise, switching median filter.**

I. Introduction

FAILURES in sensors, readout circuits, A/D converters, or communication channels may introduce impulsive noise in digital images, in particular in radiographies. Image segmentation or compression, edge detection, feature recognition, and many other image processing procedures are affected by the presence of this kind of noise. It also constitutes a serious disturbing factor when images have to be analyzed by a human observer like in clinical practice. In fact, contrast enhancement techniques such as unsharp masking (UM) [1] or gamma correction [2], drastically enhance impulsive noise and lead to poor visualization results, as shown in Fig. 1.

Linear filtering has proven inadequate to eliminate impulsive noise [3], and more elaborate solutions have been searched. Median filtering is the standard approach, since it generally achieves a complete elimination of the corrupted pixels, at least for low and medium corruption rates [3]–[7]. The peak-and-valley filter [5] uses the min and max operators to remove peaks and valleys recursively from an image; it produces an output similar to that of the median filter, but it is computationally less intensive. The drawback of these approaches is a low pass filtering effect, with consequent loss of high-frequency details of the image [3], [6]. Some adaptive versions of the median filter were proposed: they reduce this drawback, but do not completely remove it [7].

Manuscript received January 23, 2008; revised March 10, 2008. First published April 08, 2008; current version published December 24, 2008. This work was supported in part by the MIUR under Grant PRIN2006: Inverse Problems in Medicine and Astronomy. *Asterisk indicates corresponding author.*

I. Frosio is with the Computer Science Department, University of Milan, Via Comelico 39/41, 20135 Milan, Italy (e-mail: frosio@dsi.unimi.it).

*N. A. Borghese is with the Computer Science Department, University of Milan, 20135 Milan, Italy (e-mail: borghese@dsi.unimi.it).

Color versions of one or more of the figures in this paper are available online at http://ieeexplore.ieee.org.

Digital Object Identifier 10.1109/TMI.2008.922698

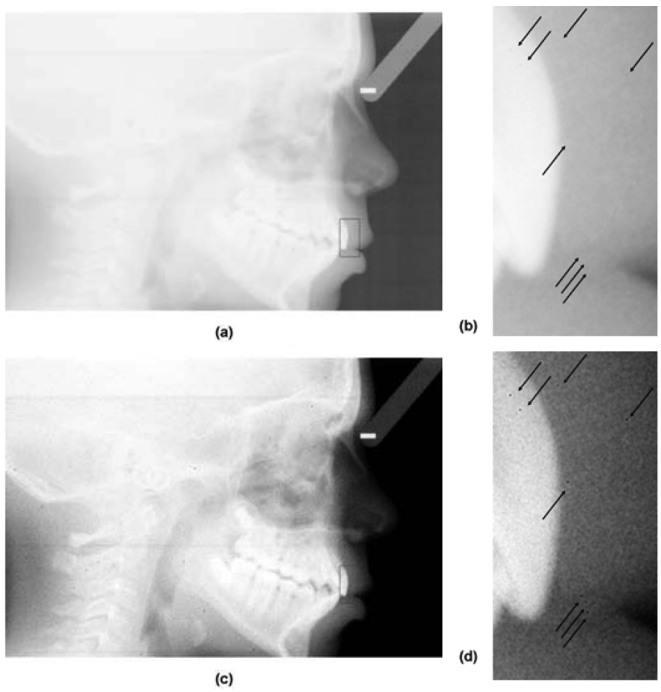

Fig. 1. Typical raw cephalometric radiography is shown in (a). Zoom of the rectangle highlighted in (a) is shown in (b): the pulses are indicated by arrows. In (c) and (d), the same radiography and the zoomed rectangle are shown after the application of gamma transform ($\gamma = 0.5$), followed by UM (mask size 3×3, gain 3): failed pixels are evident.

Better results can be obtained by resorting to a "switching filtering" scheme: the pulses are first detected and then corrected, whereas all the uncorrupted pixels remain unaltered. Pulse detection is the most critical stage in this scheme.

Some switching filters are based on rank conditioned statistics. A rank conditioned median filter (RCF) is proposed in [8]: in its simplest implementation, a median filter is turned on when the central pixel of a nxn area is the minimum (maximum) of the analyzed window. When n is small, many false pulses are found, which leads to an evident low-pass filtering effect. The problem is partially solved increasing the window size; however, in case of pulses close one to the other, several pulses go undetected.

The conditional signal adaptive median (CSAM) filter represents a more refined approach [9]; it describes the image statistics by a co-occurrence matrix, which is computed using a 3×3 window. Morphological-like operators allow computing a lower and an upper boundary for each grey level of the co-occurrence matrix. These boundaries are used to establish whether the neighbors of a pixel are "homogeneous" to it or not. A pixel is classified as a pulse on the basis of the number of homogeneous

neighbors. A postprocessing step allows the erroneously individuated pulses to be eliminated. The most critical step of the CSAM filter is the computation of the boundaries, which should be adapted to different image sizes, number of grey levels and corruption rates.

A different approach is to explicitly model the noise statistics. In [10] a Gaussian noise model is adopted to describe the local statistics; this allows both the pulses to be individuated and the true pixels value to be estimated. In [11], the predictor of a Kalman filter moves along the image computing the expected grey level of each pixel on the basis of the value of its neighbors. A pulse is identified when the prediction error is large. In this case too, the Gaussian noise approximation is required.

Mixture models have been introduced to build more refined pulse detectors. This approach works well when noise is constituted of a mixture of Gaussian and impulsive noise [13]–[15]. In [12] the Bayesian expectation maximization filter (BEM) is introduced. It describes the image locally using a Gaussian mixture model, whose number of components is automatically selected through the Akaike information criterion. The central pixel of the analyzed area is classified as a pulse and corrected when it is associated with an unlikely mixture component.

However, noise cannot be considered Gaussian in digital radiography, as its main contribution is given by the Poisson statistics of the photon counting process [16]–[20]. To the best of our knowledge, no author considered a mixture of photon counting and impulsive noise to build a pulse detector specifically tailored to digital radiography. Moreover, all the methods described in literature are not targeted to the very low corruption rates that are mandatory in this field.

In this paper, a reliable switching median filter for digital radiography is derived, taking into account the noise statistics and the properties of the sensor. It outperforms the other traditional methods. The filter has been termed RaIN, which stands for radiographic impulsive noise filter.

In Section II, the noise and the sensor model are introduced along with the method to individuate the pulses, when the noiseless image is known. In Section III, quantitative results on simulated and real images are reported. Moreover, the method is extended to the case when the noiseless image is not available, but it is obtained applying a 3×3 median filter to the measured, noisy radiography. Some theoretical considerations on the estimate of the sensor parameters are reported in Section IV. The method is discussed in Section V and conclusions are drawn in Section VI.

II. Method

A. Gain Estimate in Absence of Impulsive Noise

Let us consider a digital radiography affected by photon counting noise. Let us call $p_{n,i}$ the number of photons counted by the digital sensor in the ith pixel. This is a random variable with Poisson distribution [16]–[20]

$$p_{\mathrm{Poiss}}(p_{n,i}|p_i) = \frac{p_i^{p_{n,i}} e^{-p_i}}{p_{n,i}!} \tag{1}$$

where p_i is the noiseless photon count at pixel i.

Digital sensors transform the noisy photon count, $p_{n,i}$, into a noisy grey level value, $g_{n,i}$, by a linear transformation [21]

$$g_{n,i} = G \cdot p_{n,i} + O \tag{2}$$

where the parameter G represents the sensor gain and O its offset. As sensors are usually calibrated before their use, their output is zero, when no photons reach them (unbiased, calibrated sensor). As a consequence, in the following we will assume $O = 0$.

The probability density function of the random variable $g_{n,i}, p_{\mathrm{PC}}(g_{n,i} \,|\, g_i)$, can be derived from (1) and (2) and it is equal to [20]

$$p_{\mathrm{PC}}(g_{n,i} \,|\, g_i) = \frac{1}{G} \cdot \left[\left(\frac{g_i}{G}\right)^{\frac{g_{n,i}}{G}} e^{-\frac{g_i}{G}} \right] \Bigg/ \left[\left(\frac{g_{n,i}}{G}\right)! \right] \tag{3}$$

where g_i is the noiseless grey level of pixel i.

Let us first assume that g_i is known for each pixel of the image. The likelihood of the measured data, $L(g_{n,i} \,|\, G, g_i) = \prod_{i=1}^{N} p_{\mathrm{PC}}(g_{n,i} \,|\, g_i)$, can be derived from (3), [16], [22], [23], and it is a function of the sensor gain G. Maximization of $L(g_{n,i} \,|\, G, g_i)$ allows G to be computed, so that the observed data are the most probable, under the assumption that the image is corrupted only by photon counting noise. Instead of maximizing $L(g_{n,i} \,|\, G, g_i)$, it is easier to minimize its negative logarithm, which leads to

$$\begin{aligned} f(G) &= -\ln[L(g_{n,i} \,|\, G, g_i)] \\ &= -\ln\left[\prod_{i=1}^{N} p_{\mathrm{PC}}(g_{n,i} \,|\, g_i)\right] \\ &= -\sum_{i=1}^{N} \ln[p_{\mathrm{PC}}(g_{n,i} \,|\, g_i)] \end{aligned} \tag{4}$$

where N is the total number of pixels of the image. To minimize $f(G)$, we set to zero its derivative with respect to G. This derivative has the following expression:

$$\begin{aligned} \frac{df}{dG} &= -\sum_{i=1}^{N} \frac{d\{\ln[p_{\mathrm{PC}}(g_{n,i} \,|\, g_i)]\}}{dG} \\ &= -\sum_{i=1}^{N} \frac{d}{dG} \left\{ \ln\left(\frac{1}{G}\right) + \ln\left[\left(\frac{g_i}{G}\right)^{\frac{g_{n,i}}{G}}\right] \right. \\ &\qquad \left. + \ln\left(e^{-\frac{g_i}{G}}\right) - \ln\left[\left(\frac{g_{n,i}}{G}\right)!\right] \right\}. \end{aligned} \tag{5}$$

For the computation of the last term, the Stirling's approximation[1] of the factorial term is adopted [24]. It follows that:

$$\begin{aligned} \frac{df}{dG} \approx -\sum_{i=1}^{N} \frac{d}{dG} \left\{ -\ln(G) + \frac{g_{n,i}}{G} \cdot \ln\left(\frac{g_i}{G}\right) - \frac{g_i}{G} + \right. \\ - \frac{g_{n,i}}{G} \cdot \ln\left(\frac{g_{n,i}}{G}\right) + \frac{g_{n,i}}{G} \\ \left. - \frac{1}{2} \cdot \ln\left(\frac{g_{n,i}}{G}\right) - \ln\left(\sqrt{2\pi}\right) \right\} \end{aligned}$$

[1] $\ln(n!) \approx n \cdot \ln(n) - n + 1/2 \cdot \ln(n) + \ln(\sqrt{2\pi})$

$$= \frac{N}{2} \cdot \frac{1}{G} + \frac{1}{G^2} \cdot \sum_{i=1}^{N} \{g_{n,i} \cdot [\ln(g_i) - \ln(g_{n,i})] - g_i + g_{n,i}\}. \quad (6)$$

The value of G that minimizes (4) is obtained setting (6) to zero. It is equal to

$$G = -2/N \cdot \sum_{i=1}^{N} \{g_{n,i} \cdot [\ln(g_i/g_{n,i})] - g_i + g_{n,i}\}. \quad (7)$$

which is closely related to the Kullbach-Leibler divergence of g and g_n, or Csizar divergence [22].

B. Gain Estimate in Presence of Impulsive Noise

The image formation process has to be analyzed to derive a proper model of the noise affecting the radiographic image. The first source of noise is associated with the photon counting process. The photon count is transformed into a digital output and transmitted to a host: impulsive noise may corrupt the signal during this process. We assume that the grey level of a pulse does not depend on the grey level of the image in that pixel. The probability density function of impulsive noise will be indicated by $p_{\mathrm{Imp}}(g_{n,i})$. In this paper, a uniform distribution has been assumed for $p_{\mathrm{Imp}}(g_{n,i})$, but any other distribution can be used without affecting the following derivation.

Under the here above assumptions, we can use the following mixture model:

$$\begin{cases} p(g_{n,i} \,|\, g_i) = P_{\mathrm{PC}} \cdot p_{\mathrm{PC}}(g_{n,i} \,|\, g_i) + P_{\mathrm{Imp}} \cdot p_{\mathrm{Imp}}(g_{n,i}) \\ 0 \le P_{\mathrm{PC}} \le 1, \quad 0 \le P_{\mathrm{Imp}} \le 1, \quad P_{\mathrm{PC}} + P_{\mathrm{Imp}} = 1 \end{cases} \quad (8)$$

to describe the probability $p(g_{n,i} \,|\, g_i)$ that a pixel in the noisy image assumes the grey level $g_{n,i}$, given its true value g_i. As a consequence, a pixel has probability P_{PC} and P_{Imp} of being corrupted respectively by photon counting or impulsive noise. Since P_{PC} and P_{Imp} add to one and they are both bounded between zero and one, (8) can be rewritten as show in (9) at the bottom of the page, where γ_{PC} has been introduced to simplify the maximization of the likelihood function. In fact, the constraint $0 < P_{\mathrm{PC}} < 1$, which must hold in (8), leads to a constrained optimization. Instead, in (9) γ_{PC} is not constrained ($-\infty < \gamma_{\mathrm{PC}} < +\infty$), which leads to a simpler, unconstrained optimization problem. The price to be paid is that P_{PC} does not go to zero for finite values of γ_{PC}. However, $P_{\mathrm{PC}} > 0$ always holds for images which contain not only pixels corrupted by impulsive noise.

From (9), the negative logarithm of the likelihood can be written as a function of the two parameters γ_{PC} and G as

$$\begin{aligned} f(G, \gamma_{\mathrm{PC}}) &= -\sum_{i=1}^{N} \ln [p(g_{n,i} \,|\, g_i)] \\ &= -\sum_{i=1}^{n} \ln \left\{ e^{-\gamma_{\mathrm{PC}}^2} \cdot p_{\mathrm{PC}}(g_{n,i} \,|\, g_i) + \left[1 - e^{-\gamma_{\mathrm{PC}}^2}\right] \cdot p_{\mathrm{Imp}}(g_{n,i}) \right\} \\ &= -\sum_{i=1}^{n} \ln \left\{ \frac{e^{-\gamma_{\mathrm{PC}}^2}}{G} \cdot \left[\left(\frac{g_i}{G}\right)^{\frac{g_{n,i}}{G}} \cdot e^{-\frac{g_i}{G}} \right] \Big/ \left[\left(\frac{g_{n,i}}{G}\right)! \right] + \left[1 - e^{-\gamma_{\mathrm{PC}}^2}\right] \cdot p_{\mathrm{Imp}}(g_{n,i}) \right\}. \end{aligned} \quad (10)$$

Using again the Stirling's approximation, (10) becomes (11), as shown at the bottom page.

Let us define the following quantities in (11):

$$\begin{cases} H_i = 1/\sqrt{2\pi \cdot g_{n,i}} \\ Q_i = g_i^{g_{n,i}} \cdot g_{n,i}^{-g_{n,i}} \cdot e^{g_{n,i} - g_i} \end{cases}. \quad (12)$$

.

We observe that the computation of Q_i can easily overflow or underflow the representation capacity of a computer (for instance, for $g_i = 255$, any value $g_{n,i} > 128$ produces overflow in double precision IEEE754 format). To avoid this, instead of computing Q_i directly, we compute it as

$$Q_i = e^{\ln(Q_i)} = \exp \{g_{n,i} \cdot [\ln(g_i) - \ln(g_{n,i})] + g_{n,i} - g_i\}. \quad (13)$$

Defining

$$K_i = g_{n,i} \cdot [\ln(g_i) - \ln(g_{n,i})] + g_{n,i} - g_i \quad (14)$$

$$\begin{cases} p(g_{n,i} \,|\, g_i) = e^{-\gamma_{\mathrm{PC}}^2} \cdot p_{\mathrm{PC}}(g_{n,i} \,|\, g_i) + \left[1 - e^{-\gamma_{\mathrm{PC}}^2}\right] \cdot p_{\mathrm{Imp}}(g_{n,i}) \\ P_{\mathrm{PC}} = e^{-\gamma_{\mathrm{PC}}^2}, \; P_{\mathrm{Imp}} = 1 - P_{\mathrm{PC}} = 1 - e^{-\gamma_{\mathrm{PC}}^2} \end{cases} \quad (9)$$

$$\begin{aligned} f(G, \gamma_{\mathrm{PC}}) &\approx -\sum_{i=1}^{n} \ln \left\{ \frac{\frac{e^{-\gamma_{\mathrm{PC}}^2}}{G} \cdot \left(\frac{g_i}{G}\right)^{\frac{g_{n,i}}{G}} \cdot e^{-\frac{g_i}{G}}}{\sqrt{2\pi} \cdot \left(\frac{g_{n,i}}{G}\right)^{\frac{g_{n,i}}{G} + \frac{1}{2}} \cdot e^{-\frac{g_{n,i}}{G}}} + \left[1 - e^{-\gamma_{\mathrm{PC}}^2}\right] \cdot p_{\mathrm{Imp}}(g_{n,i}) \right\} \\ &= -\sum_{i=1}^{n} \ln \left\{ \frac{e^{-\gamma_{\mathrm{PC}}^2}}{\sqrt{2\pi \cdot g_{n,i}}} \cdot G^{-\frac{1}{2}} \cdot \left(g_i^{g_{n,i}} \cdot g_{n,i}^{-g_{n,i}} \cdot e^{g_{n,i} - g_i} \right)^{\frac{1}{G}} + \left[1 - e^{-\gamma_{\mathrm{PC}}^2}\right] \cdot p_{\mathrm{Imp}}(g_{n,i}) \right\} \end{aligned} \quad (11)$$

we obtain

$$Q_i = e^{K_i}. \tag{15}$$

By this transformation, we can now compute Q_i without risk of overflow or underflow (for instance for $g_i = 255$ and $g_{n,i} = 254$, we obtain $K_i = -0.001963$ and $Q_i = 0.9980$).

The negative logarithm of the likelihood can now be rewritten for the mixture defined in (9) as

$$f(G,\gamma_{\mathrm{PC}}) \approx -\sum_{i=1}^{n} \ln\left\{ e^{-\gamma_{\mathrm{PC}}^2} \cdot H_i \cdot G^{-\frac{1}{2}} \cdot e^{\frac{K_i}{G}} + \left[1 - e^{-\gamma_{\mathrm{PC}}^2}\right] \cdot p_{\mathrm{Imp}}(g_{n,i}) \right\}. \tag{16}$$

The gain parameter cannot be directly computed from (16) and an iterative optimization scheme has to be adopted. Classical gradient method plus line search has been adopted here, but any other optimization procedure can be used [25]–[27]. This requires the computation of the derivatives of (16) with respect to G and γ_{PC}. To the scope, we compare (16) with (10), and obtain

$$p_{\mathrm{PC}}(g_{n,i}|g_i) \approx H_i \cdot G^{-\frac{1}{2}} \cdot e^{\frac{K_i}{G}}. \tag{17}$$

Deriving (16) with respect to G and γ_{PC}, and plugging (17) into the derivatives, we obtain (see Appendix A):

$$\begin{cases} \frac{\partial f(G,\gamma_{\mathrm{PC}})}{\partial G} \approx e^{-\gamma_{\mathrm{PC}}^2} \cdot G^{-1} \cdot \sum_{i=1}^{N} \left[\frac{p_{\mathrm{PC}}(g_{n,i}|g_i)}{p(g_{n,i}|g_i)} \cdot \left(\frac{1}{2} + \frac{K_i}{G}\right) \right] \\ \frac{\partial f(G,\gamma_{\mathrm{PC}})}{\partial \gamma_{\mathrm{PC}}} \approx 2 \cdot \gamma_{\mathrm{PC}} \cdot e^{-\gamma_{\mathrm{PC}}^2} \cdot \sum_{i=1}^{N} \left[\frac{p_{\mathrm{PC}}(g_{n,i} \mid g_i) - p_{\mathrm{Imp}}(g_{n,i})}{p(g_{n,i} \mid g_i)} \right] \end{cases}. \tag{18}$$

Equations (18) can be used to minimize (16), and to obtain the gain parameter and the impulsive noise corruption rate. The terms H_i and K_i do not depend on G and γ_{PC}; therefore, they can be computed only once from $g_{n,i}$ and g_i.

Once the parameters G and γ_{PC} have been estimated, the mixture model can be used to drive a switching median filter, aimed at removing impulsive noise from the image. Impulses are identified minimizing the classification error; therefore, all those pixels which satisfy the following condition:

$$[P_{\mathrm{PC}} \cdot p_{\mathrm{PC}}(g_{n,i}|g_i)] < [P_{\mathrm{Imp}} \cdot p_{\mathrm{Imp}}(g_{n,i})] \tag{19}$$

are classified as pulses. Afterwards these pixels are corrected using the switching median filtering scheme.

III. Results

A. Estimate of g_i

The noiseless image g_i is generally not available. This section shows experimentally that the image obtained filtering $g_{n,i}$ through a 3×3 median filter, can be used instead of g_i without affecting the pulse recognition capability.

Therefore, we define

$$\tilde{g}_i = \mathrm{Median}_{3\times 3}(g_{n,i}). \tag{20}$$

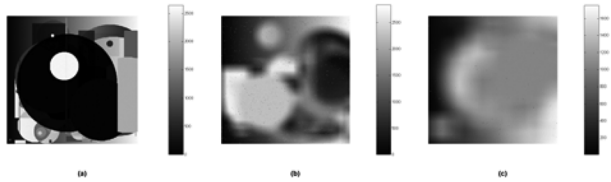

Fig. 2. Three simulated radiographies used to quantify the performance of the proposed filter: in (a), a high-frequency image with no impulsive noise; in (b), a mean frequency image (filtering by a 21×21 mask) corrupted by 1% of impulsive noise; in (c), a low-frequency image (filtering by a 49×49 mask) corrupted by 0.1% of impulsive noise.

Given the typical low corruption rate of digital radiographies and the properties of the median filter, no pulse is present in $\tilde{g}_i$.

B. Results on Simulated Images

We have generated a set of 200 simulated radiographies of 512×512 pixels. First, an absorption coefficients map is created, with coefficients increasing from 0% for the left-most pixel to 100% for the right-most one. Then, 50 different geometrical figures (circles and rectangles), randomly positioned inside the map, are added. The circles have a random radius between 1 and 512 pixels; the rectangles sides have a random length between 1 and 512 pixels. Each time a circle or a rectangle is added to the map, all the absorption coefficients covered by the figure are modified as follows: either they are substituted by their complements with respect to 100%, or they are multiplied by a random value between 0 and 1, or a random value between 0% and 100% is added to them. In the latter case, the resulting absorption coefficients are always clipped to 100%. The choice among the three modalities is random.

The map is then filtered with a moving average (MA) filter, whose window size ranges from 3×3 to 49×49, to simulate radiographies with different frequency content (Fig. 2). Depending on the size of the MA filter, the images have been grouped into three sets: high-frequency (HF) images (no filtering or filtering mask size up to 15×15 pixels [Fig. 2(a)]), medium-frequency (MF) images (mask size from 17×17 to 31×31 [Fig. 2(b)]), and low-frequency (LF) images (mask size from 33×33 to 49×49 [Fig. 2(c)]). To compute the number of photons reaching each pixel, it is supposed that the X-ray tube emits 10 000 photons per pixel area; this value is similar to that used in low dose panoramic and cephalometric imaging. Photon counting noise is added independently for each pixel, according to Poisson statistics. Photon count is then transformed into a digital output through (2) with a random gain selected between 0.05 and 0.5. The resulting sensor output, for the noiseless images, ranges between 500 and 5000 grey levels.

Impulsive noise is then introduced into the image with a pulse rate in the range between 0.01% and 1%, which corresponds to a number of pulses between 26 and 2621 per image. All the pixels have the same probability of being corrupted by impulsive noise; whether corrupted by impulsive noise, a pixel assumes a random value uniformly distributed between 0 and the maximum grey level of the image.

TABLE I
SELECTIVITY OF THE TESTED FILTERS MEASURED ON THE SIMULATED DATASET, FOR DIFFERENT IMPULSIVE CORRUPTION RATES AND IMAGE FREQUENCY CONTENTS

Se								
RCF 3x3	*Pulses%*	*0.01%*	*0.02%*	*0.05%*	*0.1%*	*0.2%*	*0.5%*	*1%*
	HF images	95.38%±4.82%	93.34%±2.05%	95.72%±1.62%	96.15%±1.03%	95.69%±1.00%	94.14%±0.89%	93.08%±0.98%
	MF images	97.23%±1.72%	97.97%±1.56%	95.74%±1.71%	95.43%±1.59%	95.75%±0.83%	95.58%±0.49%	93.74%±0.31%
	LF images	94.84%±5.83%	95.88%±3.84%	96.79%±1.59%	96.70%±0.82%	96.29%±1.22%	95.41%±0.80%	94.32%±0.57%
RCF 13x13	*Pulses%*	*0.01%*	*0.02%*	*0.05%*	*0.1%*	*0.2%*	*0.5%*	*1%*
	HF images	84.45%±3.93%	75.52%±4.32%	79.24%±3.84%	79.00%±3.71%	74.39%±3.37%	62.58%±2.72%	51.03%±3.53%
	MF images	85.19%±9.94%	87.68%±4.06%	82.01%±3.76%	80.11%±2.24%	77.45%±1.42%	66.67%±2.11%	54.40%±1.57%
	LF images	82.15%±6.36%	85.35%±6.32%	85.44%±2.78%	83.63%±1.66%	79.87%±1.94%	69.61%±1.93%	57.18%±1.88%
CSAM	*Pulses%*	*0.01%*	*0.02%*	*0.05%*	*0.1%*	*0.2%*	*0.5%*	*1%*
	HF images	82.80%±9.21%	75.24%±5.03%	79.94%±7.94%	81.39%±5.74%	81.67%±5.03%	80.52%±3.80%	79.53%±5.35%
	MF images	88.28%±6.12%	89.25%±3.52%	84.81%±3.25%	85.98%±1.19%	86.15%±1.92%	86.38%±1.81%	85.57%±1.02%
	LF images	84.68%±9.01%	86.64%±6.21%	87.26%±4.42%	88.20%±1.61%	87.12%±2.32%	87.22%±1.01%	87.28%±1.30%
UM+BEM	*Pulses%*	*0.01%*	*0.02%*	*0.05%*	*0.1%*	*0.2%*	*0.5%*	*1%*
	HF images	90.81%±5.91%	84.85%±4.63%	88.25%±2.78%	87.43%±3.63%	88.91%±2.20%	86.07%±1.80%	82.83%±3.55%
	MF images	90.78%±7.05%	92.75%±3.83%	89.31%±3.60%	89.09%±0.93%	88.74%±2.06%	88.26%±1.41%	85.77%±1.20%
	LF images	86.95%±7.51%	89.68%±5.51%	88.95%±3.51%	90.06%±2.30%	89.64%±1.69%	89.10%±1.08%	87.21%±0.68%
RaIN	*Pulses%*	*0.01%*	*0.02%*	*0.05%*	*0.1%*	*0.2%*	*0.5%*	*1%*
	HF images	94.59%±5.50%	90.61%±2.76%	94.08%±1.40%	95.21%±1.71%	95.65%±1.58%	94.83%±1.04%	94.52%±0.41%
	MF images	93.80%±4.49%	96.72%±2.34%	93.22%±1.97%	94.08%±1.44%	94.28%±1.70%	94.80%±0.96%	95.05%±0.47%
	LF images	91.78%±5.65%	92.64%±5.76%	93.67%±2.71%	94.27%±1.06%	93.96%±1.58%	94.52%±0.68%	94.70%±0.70%

TABLE II
POSITIVE PREDICTIVE VALUE OF THE TESTED FILTERS MEASURED ON THE SIMULATED DATASET, FOR DIFFERENT IMPULSIVE CORRUPTION RATES AND IMAGE FREQUENCY CONTENTS

PPV								
RCF 3x3	*Pulses%*	*0.01%*	*0.02%*	*0.05%*	*0.1%*	*0.2%*	*0.5%*	*1%*
	HF images	0.12%±0.03%	0.23%±0.07%	0.60%±0.15%	1.26%±0.47%	2.38%±0.40%	5.35%±0.88%	9.94%±1.54%
	MF images	0.13%±0.03%	0.27%±0.08%	0.61%±0.09%	1.43%±0.23%	2.51%±0.48%	6.84%±2.32%	11.45%±1.34%
	LF images	0.11%±0.04%	0.20%±0.04%	0.53%±0.15%	1.00%±0.11%	2.09%±0.33%	5.12%±0.63%	8.85%±0.94%
RCF 13x13	*Pulses%*	*0.01%*	*0.02%*	*0.05%*	*0.1%*	*0.2%*	*0.5%*	*1%*
	HF images	4.74%±1.76%	8.16%±3.07%	19.51%±7.86%	33.31%±11.72%	47.52%±7.58%	68.87%±6.46%	80.82%±4.21%
	MF images	7.04%±2.77%	15.77%±4.75%	32.27%±7.97%	49.61%±9.05%	64.10%±12.29%	85.47%±5.01%	92.18%±2.61%
	LF images	9.13%±4.05%	19.50%±7.70%	39.80%±9.29%	54.74%±10.37%	77.04%±6.65%	89.69%±3.71%	94.17%±2.64%
CSAM	*Pulses%*	*0.01%*	*0.02%*	*0.05%*	*0.1%*	*0.2%*	*0.5%*	*1%*
	HF images	21.91%±13.91%	27.70%±26.75%	35.44%±24.13%	62.07%±28.16%	77.73%±25.51%	76.70%±25.03%	88.56%±8.51%
	MF images	33.51%±22.23%	33.89%±26.21%	57.06%±27.63%	68.15%±22.86%	78.20%±22.19%	86.38%±13.12%	94.24%±6.43%
	LF images	22.25%±25.27%	28.22%±27.24%	35.80%±24.26%	41.52%±24.77%	57.63%±26.63%	81.38%±12.67%	87.65%±11.35%
UM+BEM	*Pulses%*	*0.01%*	*0.02%*	*0.05%*	*0.1%*	*0.2%*	*0.5%*	*1%*
	HF images	14.21%±2.35%	23.82%±5.70%	44.79%±9.48%	63.32%±11.03%	77.35%±3.86%	89.26%±6.03%	95.61%±0.98%
	MF images	13.40%±2.96%	25.09%±6.31%	42.26%±6.47%	65.72%±9.62%	78.27%±5.36%	91.15%±2.95%	96.54%±0.92%
	LF images	11.60%±4.89%	20.25%±4.93%	39.83%±10.45%	55.69%±4.49%	74.01%±4.55%	89.66%±2.23%	94.93%±1.12%
RaIN	*Pulses%*	*0.01%*	*0.02%*	*0.05%*	*0.1%*	*0.2%*	*0.5%*	*1%*
	HF images	41.22%±33.31%	47.35%±29.52%	60.32%±27.50%	72.44%±22.06%	82.37%±11.41%	85.55%±9.18%	90.32%±4.87%
	MF images	89.81%±10.11%	91.59%±4.67%	94.16%±4.86%	96.13%±1.90%	96.61%±1.12%	97.83%±1.19%	97.60%±0.80%
	LF images	94.82%±5.85%	95.29%±4.11%	96.78%±2.16%	97.55%±0.99%	97.61%±0.70%	98.05%±0.37%	98.32%±0.34%

In each image, we have identified the pulses through (19), using $\tilde{g}_i$, instead of g_i, as in (20). Once the corrupted pixels have been identified, they are substituted by the median value of the 3×3 window centred in those pixels, as required by the switching median filtering scheme.

To get a quantitative evaluation of the method, we adopted the following indexes [28]: selectivity (Se), specificity (Sp), positive predictive value (PPV), and negative predictive value (NPV), defined as

$$\mathrm{Se} = \frac{\mathrm{TP}}{\mathrm{TP} + FN}, \quad Sp = \frac{\mathrm{TN}}{\mathrm{FP} + \mathrm{TN}},$$
$$\mathrm{PPV} = \frac{\mathrm{TP}}{\mathrm{TP} + \mathrm{FP}}, \quad \mathrm{NPV} = \frac{\mathrm{TN}}{\mathrm{FN} + \mathrm{TN}}, \tag{21}$$

where a pixel is a true positive (TP) [or, respectively, true negative (TN)] if it is correctly classified as a pulse (or, respectively, not a pulse). A pixel which is erroneously classified as a pulse by the algorithm is called a false positive (FP); vice versa, an unrecognized pulse constitutes a false negative (FN).

Se and PPV are reported in Tables I and II, for the RCF 3×3, the RCF 13×13 [8], the CSAM [9], the BEM [12] and the RaIN filters and for different corruption rates and image frequency contents. Since the performance of the BEM filter has been verified to increase when applied after UM, we applied UM to each image before processing it with BEM. The parameters Sp and NPV are not reported since they are, respectively, smaller than 0.1% and higher than 99.9% for all the analyzed methods.

The RaIN filter is capable of localizing more than 90% of the pulses, for all the frequency contents and pulse corruption rates; Se is higher than 91% for LF images with low corruption rates ($\leq 0.2\%$), that are typical of the radiographic domain. A qualitative analysis of the undetected pulses reveals that these are compatible with the statistics of photon counting noise: their classification as pulses can be questioned, since even a human observer could not distinguish them. The PPV is always higher than 94% for LF images, but it decreases for HF images. This phenomenon can be explained considering that some edge pixels may

TABLE III
MEAN ± STANDARD DEVIATION OF CORRECTED PIXELS AND MEAN SCORES FOR THE SET OF REAL RADIOGRAPHIES ANALYZED BY THE SUBJECTS

	Unfiltered	*RCF, 3x3*	*RCF, 13x13*	*CSAM*	*UM+BEM*	*RaIN*
R_{Imp} (Mean+/-Std)	- - -	4.73% +/- 1.10%	0.23% +/- 0.08%	1.67% +/- 1.35%	0.80% +/- 0.14%	0.14% +/- 0.05%
Score (mean)	2.69	1.15	1.35	0.65	0.79	0.15

be confused with impulsive noise when edges become sharp. This problem has been addressed with *ad hoc* techniques in general-purpose pulse removal filters [9], [29]. However, as edges in radiography are never as sharp as in natural images, additional processing is not required. PPV decreases also for extremely low corruption rates: in this case the number of pulses is low and the estimate of the pulse corruption rate (P_{Imp}) becomes less reliable, affecting the performance of the pulse detector. However, for corruption rates as low as 0.01%, for LF and MF images, the RaIN filter achieves a mean PPV of 90%, meaning that less than three pixels per image, on the average, are erroneously recognized as pulses.

The RaIN filter compares favourably with the other methods. The RCF 3×3 filter achieves a slightly higher Se, which is constant for different frequency contents. However, its PPV is extremely low confirming the poor ability of this filter to discriminate the pulses. In the best case (LF images corrupted by impulsive noise of 1%, corresponding to 2621 pulses) the PPV is equal to 11.45%: 19 004 pixels are erroneously filtered, leading to a potentially unacceptable image modification rate. Increasing the filter width to 13×13, the PPV increases (for instance, it raises from 2.09% to 77.04% for LF images corrupted by impulsive noise of 0.2%), at the expense of a decrease in the ability to locate the pulses (Se drops from 96.29% to 79.87% on the same data). Moreover, differently from the proposed method, Se and PPV are both influenced by the corruption rate; this happens because the probability of finding more than one pulse inside a window increases with the impulsive corruption rate and the filter corrects only the most evident pixel inside the window.

The Se of the CSAM filter does not show any correlation with the image frequency content, but it is lower than RaIN. Moreover, its PPV is very low, for very low impulsive corruption rates (22.25% for LF images corrupted by 0.01% of impulsive noise), and it approaches 90% only for high corruption rates (1%). The BEM filter produces a behaviour similar to CSAM, with a slightly higher Se, and a PPV increasing with the corruption rate.

C. Results on Real Images

The different performances of the RaIN filter and the other ones are even more evident when real images are taken under consideration. To the scope we considered a set of 16 cephalometric images, 2437×1561 pixels, and 10 panoramic images, 1310×2534 pixels, at 12 bpp, acquired using the Orthoralix 9200 DDE by Gendex Dental System, with a corruption rate not exceeding 0.2%. Coherently with the clinical practice, each image was treated to enhance its contrast with a gamma transform $(\gamma = 0.5)$ followed by UM (mask size 3×3, gain 3). Pulses are clearly visible on these images, as shown in Fig. 1(d). Each radiography was processed with a RCF, using a 3×3 and a 13×13 window, and with the CSAM, UM+BEM, and RaIN

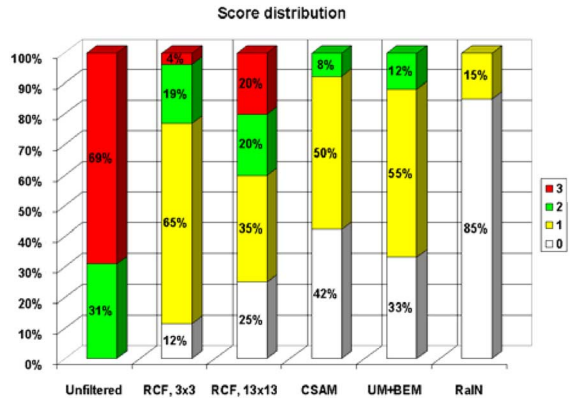

Fig. 3. Score distribution for different filters, for the set of real radiographies analyzed by the subjects.

filters. A total of 156 images were obtained, including the original unfiltered images; these constitute our test images data set.

The filtered radiographies were analyzed by 15 skilled people to evaluate the residual corruption rate of the images; seven of them were clinicians operating in the dental radiographic field, with at least three years of experience; the others were high level technicians employed in the dental radiographic field, with at least five years of experience. Fifteen images, randomly chosen from the test image data set, were shown sequentially to each subject, with the aim of assessing the presence of pulses. The subject had unlimited time to evaluate each radiography; he was free to navigate it, zooming at a constant zoom factor (8x) to better analyze the image locally. Each subject assigned a score between 0 and 3 to each analyzed image: 0, if no pulse was visible in any analyzed area (uncorrupted image); 1, if no more than two pulses were found in no more than two areas (low corruption rate); 2, if no more than two pulses were found in two or more areas (medium corruption rate); and 3, when more than two pulses were found in at least one area (high corruption rate). The subjects were briefly trained before the experiment by showing them three images with the three different levels of impulsive noise.

The mean score achieved by each filter is reported in Table III, together with the mean and standard deviation of the pixel correction rate, R_{Imp}. In Fig. 3, the distribution of the scores is shown.

All the original radiographies received a score of 2 or 3 indicating that, despite the low corruption rate, impulsive noise did appear on the displayed images. On the other hand, very few pulses were visible in the radiographies treated with the RaIN filter: the average score received was of 0.15, with 85% of the radiographies classified as 0 (not corrupted by impulsive noise). Moreover, RaIN corrected a very low number of pixels: 0.14% of the total number of pixels on the average. When the images were treated with RCF 3×3, the mean rate of corrected pixels

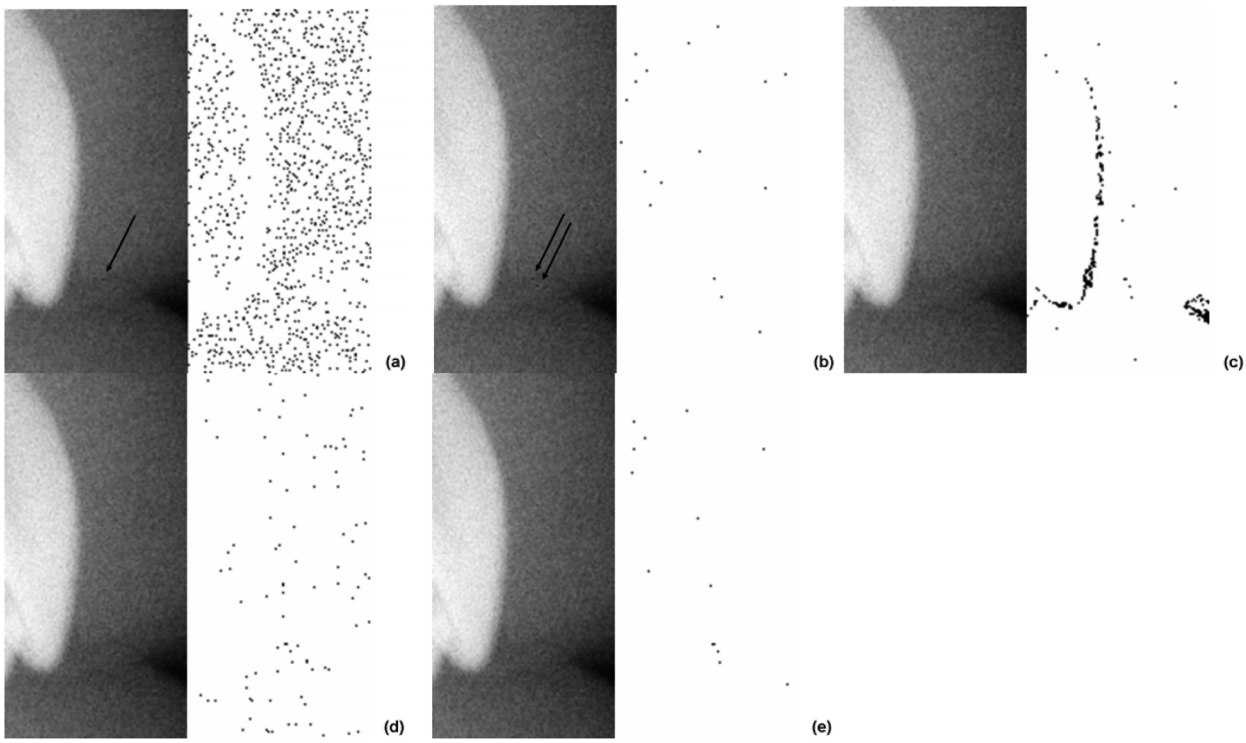

Fig. 4. Portion of radiography highlighted in Fig. 1(d) is shown here, after filtering it with the RCF using a 3×3 window (a), with the RCF using a 13×13 window (b), with the CSAM filter (c), with the UM+BEM filter (d) and with the RaIN filter (e). A γ transform ($\gamma = 0.5$) followed by UM with mask size 3×3 and gain 3 was applied to the images. The arrows in (a) and (b) indicate some of the pixels clearly corrupted by impulsive noise, but left unaltered by the RCF filters. In the right area of each panel, the pixels modified by the filter are shown.

increased to 4.73%; despite this, the filter was not able to remove the impulsive noise completely from the images as the mean score achieved by this filter was 1.15; most (65%) of the images treated with RCF 3×3 were scored as 1 and few of them (4%) received a completely unsatisfactory score of 3. The RCF 13×13 corrected a lower number of pulses (0.23% of the total number of pixels), but it left a higher number of pulses undetected (mean score of 1.35, the major part of the radiographies have been scored 1). The CSAM and the BEM filters showed similar performances; they both corrected few pixels (1.67% for CSAM, 0.80% for $\mathrm{UM} + \mathrm{BEM}$), but they both failed to remove all the pulses: their mean scores were respectively of 0.65 and 0.79, much higher than *RaIN*. A few radiographies (respectively 8% and 12%) have been scored 2 for both filters. The different behavior of the analyzed filters is evident comparing the results obtained on the same portion of image [Fig. 1(d) and Fig. 4]. The CSAM, UM+BEM, and RaIN filters are able to remove the impulsive noise completely in this area, whereas the RCF filter leaves one (3×3 window) or two (13×13 window) pulses. Moreover, RCF 3×3 corrects a large number of pixels (1035 on a total of 20 000 pixels) mainly in the homogeneous areas, whereas it does not alter the image close to the edges [Fig. 4(a)]; the same filter, using a 13×13 window, modifies a smaller number of pixels, but it also fails to identify two pulses [Fig. 4(b)]. The CSAM filter corrects all the most evident pulses, but it also filters many pixels lying on the edges of the image [Fig. 4(c)]. The BEM filter corrects all the most evident pixels, but it also filters much more uncorrupted pixels [Fig. 4(d)] than the RaIN filter [Fig. 4(e)].

D. Computational Time

The computational time required to filter the synthetic images of Section III-B, and the cephalometric and panoramic radiographies of Section III-C, was, respectively, 0.6, 7.57, and 8.48 s on a Mobile Toshiba Intel Core Duo 2-GHz, 2GB of RAM, with compiled code. The number of iteration steps was set to ten, which was sufficient to reach convergence (each estimated parameter changes less than 10^{-5} between two consecutive iterations). Computational time can be largely reduced by improving the optimization process. For instance the computational time decreases respectively to 0.21, 2.64, and 3.02 s considering only one pixel over four in the computation of the derivatives (18), for the minimization of $f(G, \gamma_{\mathrm{PC}})$.

IV. Sensor Gain Estimate

The relative error on the estimated gain parameter is depicted in Fig. 5 for the simulated dataset. It shows that the gain is underestimated for all the frequencies when the median filtered image $\tilde{g}_i$ is used in place of g_i. The relationship between the true sensor gain and $\tilde{G}$ cannot be derived because of the nonlinear nature of the median filter. We remark that the value of $\tilde{G}$ can be effectively used to locate the pulses reliably through (19), as experimentally shown in Section III. As a consequence, $\tilde{G}$ will be referred to as "equivalent gain."

Median filtering should be avoided when the true sensor gain has to be estimated; instead, linear filtering can been considered. Let us consider a radiographic image $\{g^*_{n,i}\}_{i=1\ldots N}$ corrupted only by photon counting noise. For instance, such an image

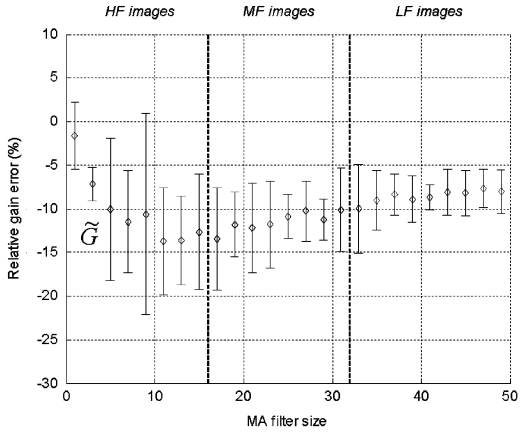

Fig. 5. Relative error of the estimate of sensor gain, for the estimates $\bar{G}$, as a function of the frequency content of the radiography. Error bars indicate three standard deviations.

could be obtained applying the procedure outlined in Section III to the original, noisy radiography. Filtering $g^*_{n,i}$ with a MA filter of size $Z \times Z$ pixels a new image, called $\hat{g}_i$, is obtained. From $g^*_{n,i}, \hat{g}_i$ and (7), an equivalent gain, $\hat{G}$, can be estimated, different from $\tilde{G}$. In this case, the following relationship between $\hat{G}$ and G can be analytically derived, at least for LF images, as shown in Appendix B (cf. B22)

$$\hat{G} \cong [(M-1)/M] \cdot G \tag{22}$$

where $M = Z^2$. Inverting (22), the sensor gain G can be computed.

This relationship can be analyzed considering for simplicity a uniform image, $g_i = \bar{g}, \quad \forall i$. In this case, from (B9) the second-order expansion of (7) can be derived

$$G \cong \frac{1}{N} \cdot \sum_{i=1}^{N} \frac{n_i^2}{g_i} = \frac{1}{N \cdot \bar{g}} \cdot \sum_{i=1}^{N} n_i^2 = \frac{1}{N \cdot \bar{g}} \cdot \sum_{i=1}^{N} (g_{n,i} - g_i)^2 \tag{23}$$

where $n_i = g_{n,i} - g_i$ is the noise contribution for the ith pixel. Expression (23) highlights that the estimated sensor gain is proportional to the noise power, $\sum_{i=1}^{N} (g_{n,i} - g_i)^2$. When g_i is substituted by $\hat{g}_i$, the low-pass filter does not completely remove the noise from the image. In particular, for a MA filter with M samples, the residual noise power is equal to $(M-1)/M$ with respect to the original power [23]. As a consequence, $\hat{G}$ underestimates the true sensor gain by a factor $1/M$, as reported in (22).

To validate this derivation, we generated a set of 26 images of 512×512 pixels, each containing a sinusoidal oscillation in the horizontal direction, with frequency between 0 and 0.025 cycles per pixel, with increments of 0.001 cycles per pixels. The minimum and maximum number of incident photons of each image was set, respectively, to 1000 and 11 000, coherently with the data used in Section III-B. For each noiseless image, ten noisy images were generated, each with a different realization of photon counting noise, for a total of 260 noisy images. Gain values compatible with real radiographic images (0.1 and 0.2)

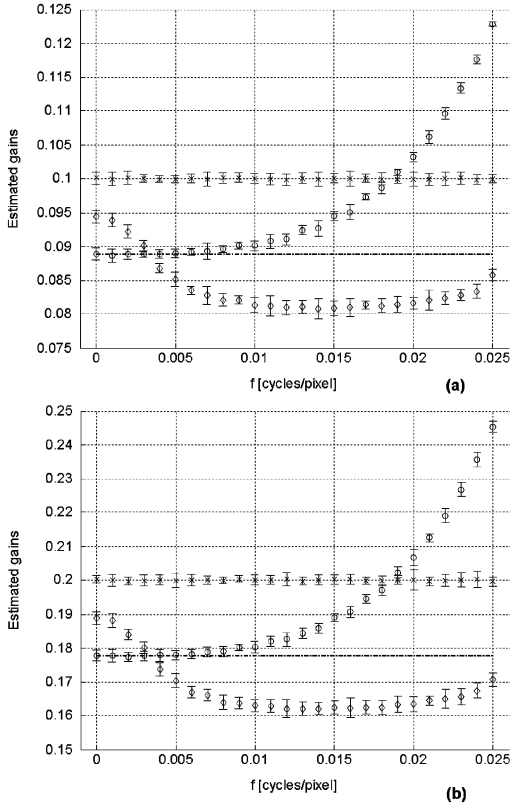

Fig. 6. Estimate of the gain parameter as a function of the frequency content, for G (crosses), $\bar{G}$ (diamonds), and $\hat{G}$ (circles). In (a), the true value of the gain parameter is 0.1; in (b), it is 0.2. Error bars indicate three standard deviations, whereas the dash–dotted horizontal line indicates the theoretical estimate of $\hat{G}$, for LF images.

have been used to generate such images. $\hat{g}_i$ and $\tilde{g}_i$ were computed, for each noisy image of the simulated dataset, using, respectively, a 3×3 MA filter and a 3×3 median filter applied to $g^*_{n,i}$. The values of $G, \hat{G}$, and $\tilde{G}$ were determined from these images and they are reported in Fig. 6.

When the true image g_i is used, the value of G is always very close to the true sensor gain with a standard deviation lower than 0.5%. This demonstrates that the Stirling's approximation used to derive (7) does not introduce any bias on the estimated gain. The behavior of $\tilde{G}$ is similar to that obtained in Fig. 5 and it does not allow G to be reliably estimated. Instead, when the MA filtered image $\hat{g}_i$ is considered, the curve obtained from (7) increases monotonically: for low-frequency values, $\hat{G}$ is very close to the theoretical value predicted by (22), 8/9 of the true sensor gain, and it increases for higher frequencies; for frequencies up to 0.005 cycles/pixel, the error on the estimated gain is smaller than 0.3% of the true gain value.

To evaluate the frequency content of the radiographies of the dataset, for each image we have computed the 2-D Fourier transform in polar coordinates, $F(\rho, \vartheta)$, and determined the power up to frequency f, $\int_0^f \int_0^{2\pi} [F(\rho,\vartheta)]^2 d\vartheta d\rho$. This value is then normalized as follows:

$$\xi(f) = 100 \cdot \left\{ \int_0^f \int_0^{2\pi} [F(\rho,\vartheta)]^2 d\vartheta d\rho \right\} \Bigg/ \left\{ \int_0^{0.5} \int_0^{2\pi} [F(\rho,\vartheta)]^2 d\vartheta d\rho \right\} \tag{24}$$

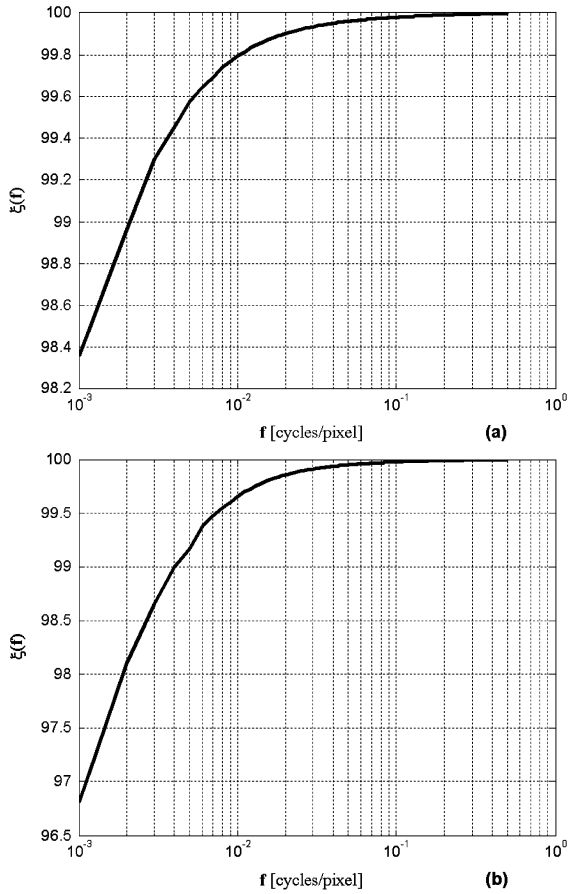

Fig. 7. Normalized cumulative power, $\xi(f)$s plotted for (a) the cephalometric radiographies and (b) the panoramic radiographies of Section III-C.

where the integral at the denominator is computed between 0 and the Nyquist frequency (0.5 cycles/pixel). The mean trend of $\xi(f)$ is plotted in Fig. 7 for the set of cephalometric and panoramic radiographies considered in Section III-C; 99.5% (for the cephalometric radiographies) and 99.2% (for the radiographic radiographies) of the power is contained inside the frequency range $f \leq 0.005$ cycles/pixel. On the basis of this result, (22) can be considered a reliable expression to compute the true sensor gain, at least for the images considered in our experiments.

For sake of completeness, for the real radiographies of our dataset, the estimated mean value ($\pm$ standard deviation) of the sensor gain was of 0.212 ± 0.025 for the cephalometric radiographies and 0.095 ± 0.003 for the panoramic radiographies.

V. Discussion

Digital radiographies are characterized by a very low impulsive noise rate: for the images analyzed here, it did not exceed 0.2%. Nevertheless, its effect on image visualization after gamma correction and UM is remarkable: all the untreated radiographies of Section III-C were classified as medium or highly corrupted by all the human observers. This clearly demonstrates the need of a filtering procedure aimed to remove the impulsive noise.

The proposed method is based on a realistic model of noise distribution and an adequate (linear) sensor model. More refined sensor models could be used, which incorporate for instance nonlinearity or histeresis [21]. However, as producers try to maximize linearity, sensors of the last generations are usually accurately described by a linear transfer function.

Whether the sensor response were not uniform, the present approach could be extended to incorporate a parametric space-varying gain map into the sensor model. This is the case, for instance, of large area sensors covered by a non uniform scintillator layer, like the ones considered in [30]. However, this problem does not arise for small area sensors and the widely used linear sensors, like those considered here [21].

A mixture of impulsive and photon counting noise has been considered, where it is supposed that impulsive noise destroys the signal. Therefore, each pixel can be affected either by photon counting or impulsive noise. Although other forms of noise could be considered, like thermal, readout, or quantization noise, for a well constructed and calibrated radiographic sensor, these are much smaller than photon counting and impulsive noise. For instance, the readout noise of the sensor used to take the images of Section III-C, is typically as small as 1/5 grey level on a total of 4096 grey levels.[2]

The photon counting noise has been assumed white. This assumption is required to derive the expressions of the likelihood functions in (4) and (10), and it is equivalent to assume that the sensor point spread function is the delta function. A more accurate description of the sensor response could be accommodated into a more complex likelihood function, at the price of a higher computational cost and of an adequate estimate procedure. However, experimental results on real images suggest that this increase in complexity does not seem justified.

The sensor transforms photon counting noise according to (3). This clearly shows that the common statement that "radiographic images are corrupted by Poisson noise" is partially misleading. The noise in the grey level image is purely Poisson only when sensor gain is unitary. Such observation should be carefully considered each time an image de-noising algorithm, specifically tailored to photon counting noise, is developed.

The Stirling's approximation of the factorial function was introduced in (6) and (11), to make (5) a continuous, differentiable function of G [32]. This approximation rapidly converges to the true value for small values of n and we have experimentally verified that it does not significantly affect the estimate of the gain parameter.

A critical step is the estimate of the noiseless image g_i. During sensor calibration, a uniform image is often taken. In this case, g_i can be assumed constant and equal to the mean (or the median) gray level of $g_{n,i}$ and the RaIN filter can be reliably used to both individuate the faulty pixels of the sensor and to estimate the sensor gain.

A more difficult problem arises when the pulses have to be identified and removed from a radiography taken on the field. In this case, we verified experimentally that the RaIN filter does identify the noise pulses reliably, provided that g_i is computed as the median filtered noisy image. The smallest possible kernel, 3×3 has been adopted. A larger kernel could be used for higher

[2]http://jp.hamamatsu.com/resources/products/ssd/pdf/s7199-01_kmpd1077e06.pdf

corruption rates, but its use is not justified for the low-corruption rates typical of radiographic images, as the computational cost increases.

The RaIN filter was compared with several among the most used filters for impulsive noise removal. The RCF filter was selected because of its computational efficiency; the CSAM filter because it estimates the noise variance as a function of the grey level, coherently with the properties of photon counting noise. For the same reason the proposed method was also compared with the BEM filter, which provides a local, model based description of the image and noise characteristic. As shown by the results, statistical methods like the RaIN, the BEM or the CSAM filters remove impulsive noise much better than the simpler RCF filter. Among these, RaIN achieves the best performance, thanks to its accurate description of the noise statistics represented in the mixture model (8). Both the CSAM and the BEM filters leave a significant number of uncorrected pulses, as shown by the relative high mean score achieved by these filters. Moreover they erroneously identify as pulses more pixels than the RaIN filter (Fig. 4). This fact can be attributed to the less realistic statistical model implemented by them. As a matter of fact, CSAM is a general purpose filter: in fact it does not adopt a parametric statistical model to describe the image statistics, but it derives it through a regularized co-occurrence matrix. On the other hand, BEM approximates the noise locally as a mixture of Gaussians.

Our experimental results demonstrate that, by improving the reliability of the noise model, a more efficient denoising algorithm can be obtained. This suggests that an accurate description of the noise statistics could lead to better results also in other domains, like in tomography, where noise is often approximated through a Gaussian distribution [31].

Beyond removing the pulses, the RaIN filter also allows to estimate the sensor gain as follows. First the pulses have to be removed with the procedure outlined in Section III; then, the gain can be estimated according to Section IV.

VI. Conclusion

We have proposed here a novel method to individuate and correct impulsive noise in digital radiography. The method is based on the assumption that the photon counting process provides the main contribution to image noise, which is a common characteristic of many radiographic systems. A mixture of photon counting and impulsive noise is used to individuate the pulses; however, any other form of noise can be easily introduced in this model. The method also allows a reliable estimate of the sensor gain. The experimental results on both simulated and real images demonstrate the superiority of the proposed method compared with other, more traditional approaches.

Appendix A

We report here the derivation of the derivatives of (16) with respect to G and γ_{PC}, show in (A1) and (A2), at the bottom of the next page.

Appendix B

Let us consider a simplified framework, where an image is corrupted only by photon counting noise. The measured noise image, $g_{n,i}$, can be written as

$$g_{n,i} = g_i + n_i \tag{B1}$$

where n_i is the photon counting noise contribution to the ith pixel. As a consequence, (7) can be rewritten as

$$\begin{aligned} G &= -\frac{2}{N}\cdot\sum_{i=1}^{N}\{(g_i+n_i)\cdot[\ln(g_i) \\ &\quad -\ln(g_i+n_i)]+(g_i+n_i)-g_i\} \\ &= -\frac{2}{N}\cdot\sum_{i=1}^{N}[g_i\cdot\ln(g_i) \\ &\quad -g_i\cdot\ln(g_i+n_i)+n_i\cdot\ln(g_i) \\ &\quad -n_i\cdot\ln(g_i+n_i)+n_i]. \end{aligned} \tag{B2}$$

The expression of G in (B2) can be approximated using its second-order Taylor expansion as

$$\begin{aligned} G(\mathbf{n}) \cong\ & G(\mathbf{n_0})+\nabla G(\mathbf{n_0})\cdot(\mathbf{n}-\mathbf{n_0}) \\ & +(1/2)\cdot(\mathbf{n}-\mathbf{n_0})\cdot H_G(\mathbf{n_0})\cdot(\mathbf{n}-\mathbf{n_0})^T \end{aligned} \tag{B3}$$

where the vector $\mathbf{n}$ contains the noise over all the pixels, $\mathbf{n} = \{n_i\}_{i=1\ldots N}$; $\nabla G(\mathbf{n_0})$ and $H_G(\mathbf{n_0})$ are the gradient and the Hessian of $G(\mathbf{n})$ and $\mathbf{n}_0$ is a vector of zeros.

Let us first compute $G(\mathbf{n}_0)$

$$\begin{aligned} G(\mathbf{n_0}) = -\frac{2}{N}\cdot\sum_{i=1}^{N}&[g_i\cdot\ln(g_i)-g_i\cdot\ln(g_i+0) \\ &+0\cdot\ln(g_i)-0\cdot\ln(g_i+0)+0]=0. \end{aligned} \tag{B4}$$

.

Computing the derivatives of (B2) with respect to $\mathbf{n}$, we obtain

$$\begin{aligned} &\nabla G(\mathbf{n})\cdot\mathbf{e_i} \\ &\quad = -\frac{2}{N}\cdot\left[-\frac{g_i}{g_i+n_i}+\ln(g_i)\right. \\ &\qquad \left.-\ln(g_i+n_i)-\frac{n_i}{g_i+n_i}+1\right] \\ &\quad = -\frac{2}{N}\cdot[\ln(g_i)-\ln(g_i+n_i)] \end{aligned} \tag{B5}$$

where $\mathbf{e}_i$ is a vector whose ith component is 1, and all the other components are 0.

For $\mathbf{n}_0 = 0$, (B5) gives

$$\nabla G(\mathbf{n_0})\cdot\mathbf{e_i} = 0 \quad \forall i. \tag{B6}$$

Deriving (B5), we obtain

$$H_G(\mathbf{n}) = \begin{bmatrix} \frac{2}{N}\cdot\frac{1}{g_1+n_1} & 0 & \cdots & 0 \\ 0 & \frac{2}{N}\cdot\frac{1}{g_2+n_2} & \cdots & \cdots \\ \cdots & \cdots & \cdots & 0 \\ 0 & \cdots & 0 & \frac{2}{N}\cdot\frac{1}{g_N+n_N} \end{bmatrix} \tag{B7}$$

that, for $\mathbf{n} = \mathbf{n}_0$, gives

$$H_G(\mathbf{n_0}) = \begin{bmatrix} \frac{2}{N} \cdot \frac{1}{g_1} & 0 & \cdots & 0 \\ 0 & \frac{2}{N} \cdot \frac{1}{g_2} & \cdots & \cdots \\ \cdots & \cdots & \cdots & 0 \\ 0 & \cdots & 0 & \frac{2}{N} \cdot \frac{1}{g_N} \end{bmatrix}. \quad \text{(B8)}$$

As a result, the Taylor expansion of $G(\mathbf{n})$ can be written as

$$G(\mathbf{n}) \cong 1/2 \cdot \mathbf{n} \cdot H_G(\mathbf{n_0}) \cdot \mathbf{n^T} = 1/N \cdot \sum_{i=1}^{N} (n_i^2/g_i). \quad \text{(B9)}$$

We now write the Taylor expansion of (7), when g_i is substituted by its estimate. Let us consider a simplified framework, where the estimated noiseless image, $\hat{g}_i$, is obtained using a MA filter with M samples, that is

$$\hat{g}_i = (1/M) \cdot \sum_{m \in \Psi(i)} g_{n,m} \quad \text{(B10)}$$

where $\Psi(i)$ indicates the set of indexes of the M neighbors of the ith pixel, including the ith pixel itself. Under the hypothesis that the image frequency content is mainly given by the low frequency components, the MA filter does not significantly modify the signal, but it only reduces the noise. In this case, (B10) can be simplified as

$$\begin{aligned} \hat{g}_i &= \frac{1}{M} \cdot \sum_{m \in \Psi(i)} (g_m + n_m) \\ &= \frac{1}{M} \cdot \sum_{m \in \Psi(i)} g_m + \frac{1}{M} \cdot \sum_{m \in \Psi(i)} n_m \\ &\cong g_i + \frac{1}{M} \cdot \sum_{m \in \Psi(i)} n_m \\ &= g_i + \frac{1}{M} \cdot n_i + \frac{1}{M} \cdot \sum_{m \in \Psi(i) \backslash i} n_m, \end{aligned} \quad \text{(B11)}$$

$$\begin{aligned} \frac{\partial f(G, \gamma_{\mathrm{PC}})}{\partial G} &\approx \frac{\partial}{\partial G} \left\{ -\sum_{i=1}^{N} \ln \left[p(g_{n,i}|g_i) \right] \right\} = -\sum_{i=1}^{N} \left[\frac{1}{p(g_{n,i}|g_i)} \cdot \frac{\partial p(g_{n,i}|g_i)}{\partial G} \right] \\ &= -\sum_{i=1}^{N} \left(\frac{1}{p(g_{n,i}|g_i)} \cdot \frac{\partial}{\partial G} \left\{ e^{-\gamma_{\mathrm{PC}}^2} \cdot p_{\mathrm{PC}}(g_{n,i}|g_i) + \left[1 - e^{-\gamma_{\mathrm{PC}}^2} \right] \cdot p_{\mathrm{Imp}}(g_{n,i}|g_i) \right\} \right) \\ &= -\sum_{i=1}^{N} \left\{ \frac{1}{p(g_{n,i}|g_i)} \cdot e^{-\gamma_{\mathrm{PC}}^2} \frac{\partial}{\partial G} [p_{\mathrm{PC}}(g_{n,i}|g_i)] \right\} \\ &= e^{-\gamma_{\mathrm{PC}}^2} \cdot \sum_{i=1}^{N} \left\{ \frac{H_i}{p(g_{n,i}|g_i)} \cdot \frac{\partial}{\partial G} \left[G^{-\frac{1}{2}} \cdot e^{\frac{K_i}{G}} \right] \right\} \\ &= -e^{-\gamma_{\mathrm{PC}}^2} \cdot \sum_{i=1}^{N} \left\{ \frac{H_i}{p(g_{n,i}|g_i)} \cdot \left[-\frac{1}{2} \cdot G^{-\frac{3}{2}} \cdot e^{\frac{K_i}{G}} + G^{-\frac{1}{2}} \cdot e^{\frac{K_i}{G}} \cdot \left(-\frac{K_i}{G^2} \right) \right] \right\} \\ &= -e^{-\gamma_{\mathrm{PC}}^2} \cdot \sum_{i=1}^{N} \left[\frac{H_i}{p(g_{n,i}|g_i)} \cdot e^{\frac{K_i}{G}} \cdot G^{-\frac{3}{2}} \cdot \left(-\frac{1}{2} - \frac{K_i}{G} \right) \right] \\ &= e^{-\gamma_{\mathrm{PC}}^2} \cdot G^{-1} \cdot \sum_{i=1}^{N} \left[\frac{p_{\mathrm{PC}}(g_{n,i}|g_i)}{p(g_{n,i}|g_i)} \cdot \left(\frac{1}{2} + \frac{K_i}{G} \right) \right] \end{aligned} \quad \text{(A1)}$$

$$\begin{aligned} \frac{\partial f(G, \gamma_{\mathrm{PC}})}{\partial \gamma_{\mathrm{PC}}} &\approx \frac{\partial}{\partial \gamma_{\mathrm{PC}}} \left\{ -\sum_{i=1}^{N} \ln \left[p(g_{n,i}|g_i) \right] \right\} \\ &= -\sum_{i=1}^{N} \left[\frac{1}{p(g_{n,i}|g_i)} \cdot \frac{\partial p(g_{n,i}|g_i)}{\partial \gamma_{\mathrm{PC}}} \right] \\ &= -\sum_{i=1}^{N} \left(\frac{1}{p(g_{n,i}|g_i)} \cdot \frac{\partial}{\partial \gamma_{\mathrm{PC}}} \left\{ e^{-\gamma_{\mathrm{PC}}^2} \cdot p_{\mathrm{PC}}(g_{n,i}|g_i) + \left[1 - e^{-\gamma_{\mathrm{PC}}^2} \right] \cdot p_{\mathrm{Imp}}(g_{n,i}|g_i) \right\} \right) \\ &= -\sum_{i=1}^{N} \left(\frac{1}{p(g_{n,i}|g_i)} \cdot \frac{\partial}{\partial \gamma_{\mathrm{PC}}} \cdot \left\{ e^{-\gamma_{\mathrm{PC}}^2} \cdot [p_{\mathrm{PC}}(g_{n,i}|g_i) - p_{\mathrm{Imp}}(g_{n,i}|g_i)] \right\} \right) \\ &= 2 \cdot \gamma_{\mathrm{PC}} \cdot e^{-\gamma_{\mathrm{PC}}^2} \cdot \sum_{i=1}^{N} \left[\frac{p_{\mathrm{PC}}(g_{n,i}|g_i) - p_{\mathrm{Imp}}(g_{n,i}|g_i)}{p(g_{n,i}|g_i)} \right]. \end{aligned} \quad \text{(A2)}$$

where the noise contribution of the ith pixel, n_i, has been highlighted and$\Psi(i)\backslash i$ indicates the set of indexes of the M neighbors of the ith pixel, excluding the ith pixel itself.

Let us rewrite (7) introducing $\hat{g}_i$ in place of g_i. We obtain

$$\begin{aligned}
\hat{G}(\mathbf{n}) &= -\frac{2}{N}\cdot\sum_{i=1}^{N}\{(g_i+n_i)\\
&\quad\cdot[\ln(\hat{g}_i)-\ln(g_i+n_i)]+g_{n,i}-\hat{g}_i\}\\
&= -\frac{2}{N}\cdot\sum_{i=1}^{N}[g_i\cdot\ln(\hat{g}_i)-g_i\cdot\ln(g_i+n_i)\\
&\quad+n_i\cdot\ln(\hat{g}_i)\\
&\quad-n_i\cdot\ln(g_i+n_i)+g_i+n_i-\hat{g}_i]\\
&\cong -\frac{2}{N}\cdot\sum_{i=1}^{N}[g_i\cdot\ln(g_i+(1/M)\cdot n_i\\
&\quad+(1/M)\cdot\sum_{m\in\Psi(i)\backslash i}n_m)\\
&\quad-g_i\cdot\ln(g_i+n_i)+n_i\cdot\ln(g_i\\
&\quad+(1/M)\cdot n_i+(1/M)\cdot\sum_{m\in\Psi(i)\backslash i}n_m)\\
&\quad-n_i\cdot\ln(g_i+n_i)+g_i\\
&\quad+n_i-g_i-(1/M)\cdot n_i-(1/M)\cdot\sum_{m\in\Psi(i)\backslash i}n_m\Bigg]\\
&= -\frac{2}{N}\cdot\sum_{i=1}^{N}g_i\cdot\ln\\
&\quad\left(g_i+(1/M)\cdot n_i+(1/M)\cdot\sum_{m\in\Psi(i)\backslash i}n_m\right)\\
&\quad+\frac{2}{N}\cdot\sum_{i=1}^{N}g_i\cdot\ln(g_i+n_i)-\frac{2}{N}\cdot\sum_{i=1}^{N}n_i\\
&\quad\cdot\ln\left(g_i+(1/M)\cdot n_i+(1/M)\cdot\sum_{m\in\Psi(i)\backslash i}n_m\right)\\
&\quad+\frac{2}{N}\cdot\sum_{i=1}^{N}n_i\cdot\ln(g_i+n_i)-\frac{2}{N}\cdot(1-(1/M))\\
&\quad\cdot\sum_{i=1}^{N}n_i+\frac{2}{N}\cdot(1/M)\cdot\sum_{i=1}^{N}\sum_{m\in\Psi(i)\backslash i}n_m.
\end{aligned}\tag{B12}$$

Let us consider the second-order Taylor expansion also of $\hat{G}(\mathbf{n})$. Its first term, for $\mathbf{n}=\mathbf{n}_0=0$, is equal to

$$\hat{G}(\mathbf{n_0})=0. \tag{B13}$$

To compute the second term, the derivative of $\hat{G}(\mathbf{n})$ with respect to the ith component of $\mathbf{n}$ are computed. They are

$$\begin{aligned}
&\nabla\hat{G}(\mathbf{n})\cdot\mathbf{e_i}\\
&\quad=-\frac{2}{N}\cdot\frac{1}{M}\cdot\frac{g_i}{g_i+\frac{1}{M}\cdot n_i+\frac{1}{M}\cdot\sum_{m\in\Psi(i)\backslash i}n_m}\\
&\quad\quad-\frac{2}{N}\cdot\frac{1}{M}\\
&\quad\quad\cdot\sum_{m\in\Psi(i)\backslash i}\frac{g_m}{g_m+\frac{1}{M}\cdot n_i+\frac{1}{M}\cdot\sum_{k\in\Psi(m)\backslash i}n_k}\\
&\quad\quad+\frac{2}{N}\cdot\frac{g_i}{g_i+n_i}-\frac{2}{N}\cdot\ln\\
&\quad\quad\left(g_i+\frac{1}{M}\cdot n_i+\frac{1}{M}\cdot\sum_{m\in\Psi(i)\backslash i}n_m\right)\\
&\quad\quad-\frac{2}{N}\cdot\frac{1}{M}\cdot\frac{n_i}{g_i+\frac{1}{M}\cdot n_i+\frac{1}{M}\cdot\sum_{m\in\Psi(i)\backslash i}n_m}\\
&\quad\quad-\frac{2}{N}\cdot\frac{1}{M}\\
&\quad\quad\cdot\sum_{m\in\Psi(i)\backslash i}\frac{n_m}{g_m+\frac{1}{M}\cdot n_i+\frac{1}{M}\sum_{k\in\Psi(m)\backslash i}n_k}\\
&\quad\quad\cdot\frac{2}{N}\cdot\ln(g_i+n_i)+\frac{2}{N}\cdot\frac{n_i}{g_i+n_i}-\frac{2}{N}\\
&\quad\quad\cdot\left(1-\frac{1}{M}\right)+\frac{2}{N}\cdot\frac{1}{M}\cdot(M-1)\\
&\quad=-\frac{2}{N}\cdot\Bigg[\frac{1}{M}\cdot\frac{g_i+n_i}{g_i+\frac{1}{M}\cdot n_i+\frac{1}{M}\cdot\sum_{m\in\Psi(i)\backslash i}n_m}\\
&\quad\quad+\frac{1}{M}\cdot\sum_{m\in\Psi(i)\backslash i}\frac{g_m+n_m}{g_m+\frac{1}{M}\cdot n_i+\frac{1}{M}\cdot\sum_{k\in\Psi(m)\backslash i}n_k}\\
&\quad\quad+\ln\left(g_i+\frac{1}{M}\cdot n_i+\frac{1}{M}\cdot\sum_{m\in\Psi(i)\backslash i}n_m\right)\\
&\quad\quad-\ln(g_i+n_i)-1]
\end{aligned}\tag{B14}$$

which, for $\mathbf{n}=\mathbf{n}_0=0$, gives

$$\begin{aligned}
&\nabla\hat{G}(\mathbf{n_0})\cdot\mathbf{e_i}\\
&\quad=-(2/N)\cdot[(1/M)+(1/M)\\
&\quad\quad\cdot\sum_{m\in\Psi(i)\backslash i}g_m/g_m+\ln(g_i)-\ln(g_i)-1\Bigg]\\
&\quad=-(2/N)\cdot[(1/M)+(M-1)/M\\
&\quad\quad+\ln(g_i)-\ln(g_i)-1]=0
\end{aligned}\tag{B15}$$

and therefore

$$\nabla\hat{G}(\mathbf{n_0})=\mathbf{0}. \tag{B16}$$

Lastly, we compute the Hessian of $\hat{G}(\mathbf{n})$. Since the noise is white, n_i and n_j are uncorrelated for $i\neq j$, it can be demonstrated that only the diagonal elements of the Hessian are different from zero in the Taylor expansion. In fact, the second-order term is

$$\begin{aligned}
&(1/2)\cdot\mathbf{n}\cdot H_{\hat{G}}\cdot\mathbf{n^T}=\\
&(1/2)\cdot\sum_{i=1}^{N}H_{\hat{G},ii}\cdot n_i^2+(1/2)\cdot\sum_{i=1}^{N}\sum_{j=1}^{N}H_{\hat{G},ij}\cdot n_i\cdot n_j.
\end{aligned}\tag{B17}$$

For a large image ($N\to\infty$) the second term in (B17) vanishes, since n_i and n_j are uncorrelated. Therefore, the following relationship holds:

$$(1/2)\cdot\mathbf{n}\cdot H_{\hat{G}}\cdot\mathbf{n^T}=(1/2)\cdot\sum_{i=1}^{N}H_{\hat{G},ii}\cdot n_i^2. \tag{B18}$$

We now compute the diagonal elements of $H_{\hat{G}}$. These are obtained deriving (B15) with respect to n_i, which gives

$$H_{\hat{G},ii} = -\frac{2}{N}\cdot\left[\frac{1}{M}\cdot\frac{1}{g_i+\frac{1}{M}\cdot n_i+\frac{1}{M}\cdot\sum_{m\in\Psi(i)\setminus i} n_m} - \frac{1}{M}\cdot\frac{g_i+n_i}{\left(g_i+\frac{1}{M}\cdot n_i+\frac{1}{M}\cdot\sum_{m\in\Psi(i)\setminus i} n_m\right)^2}\cdot\frac{1}{M} - \frac{1}{M}\cdot\sum_{m\in\Psi(i)\setminus i}\frac{g_m+n_m}{\left(g_m+\frac{1}{M}\cdot n_i+\frac{1}{M}\cdot\sum_{k\in\Psi(m)\setminus i} n_k\right)^2}\cdot\frac{1}{M} + \frac{1}{M}\cdot\frac{1}{g_i+\frac{1}{M}\cdot n_i+\frac{1}{M}\cdot\sum_{m\in\Psi(i)\setminus i} n_m} - \frac{1}{g_i+n_i}\right]. \quad \text{(B19)}$$

For $\mathbf{n}=\mathbf{n}_0=\mathbf{0}$, the following expression results:

$$H_{\hat{G},ii}(\mathbf{n_0}) = -\frac{2}{N}\cdot\left[\frac{1}{M\cdot g_i}-\frac{1}{M^2\cdot g_i} - \frac{1}{M^2}\sum_{m\in\Psi(i)\setminus i}\frac{1}{g_m}+\frac{1}{M\cdot g_i}-\frac{1}{g_i}\right]. \quad \text{(B20)}$$

Remembering that, according to our hypothesis, the image frequency content is mainly given by the low-frequency components, we can approximate $\sum_{m\in\Psi(i)\setminus i}\frac{1}{g_m}$ with $\frac{M-1}{g_i}$ and write

$$\begin{aligned} H_{\hat{G},ii}(\mathbf{n_0}) &\cong -\frac{2}{N}\cdot\left[\frac{1}{M\cdot g_i}-\frac{1}{M^2\cdot g_i} - \frac{M-1}{M^2\cdot g_i}+\frac{1}{M\cdot g_i}-\frac{1}{g_i}\right] = \\ &\quad -\frac{2}{N}\cdot\frac{1}{g_i}\left[\frac{M-1-M+1+M-M^2}{M^2}\right] \\ &= \frac{2}{N}\cdot\frac{M-1}{M}\cdot\frac{1}{g_i}. \end{aligned} \quad \text{(B21)}$$

We can lastly write the Taylor expansion of $\hat{G}(\mathbf{n})$ as

$$\begin{aligned} \hat{G}(\mathbf{n}) &\cong \frac{1}{2}\cdot\mathbf{n}\cdot H_{\hat{G}}(\mathbf{n_0})\cdot\mathbf{n^T} \\ &= \frac{1}{N}\cdot\frac{M-1}{M}\cdot\sum_{i=1}^{N}\frac{n_i^2}{g_i} \\ &= \frac{M-1}{M}\cdot G(\mathbf{n}). \end{aligned} \quad \text{(B22)}$$

It follows that, when g_i is approximated by $\hat{g}_i$, and g_i contains mainly low-frequency components, the sensor gain computed through (7) is underestimated by a factor $(M-1)/M$, where M is the number of samples of the MA filter used to estimated $\hat{g}_i$ from $g_{n,i}$.

ACKNOWLEDGMENT

The authors would like to thank M. Bertero and P. Boccacci for the insightful and interesting discussions.

REFERENCES

[1] Polesel, G. Ramponi, and V. J. Mathews, "Image enhancement via adaptive unsharp masking," *IEEE Trans. Image Process.*, vol. 9, no. 3, pp. 505–510, Mar. 2000.
[2] I. Frosio, G. Ferrigno, and N. A. Borghese, "Enhancing digital cephalic radiography with mixture models and local gamma correction," *IEEE Trans. Med. Imag.*, vol. 25, no. 1, pp. 113–121, Jan. 2006.
[3] O. Rioul, "A spectral Algorithm for removing salt and pepper from images," in *Proc. 1996 Digital Signal Processing Workshop*, Loen, Norway, 1996, pp. 275–278.
[4] I. Aizenberg, C. Butakoff, and Paily, "Impulsive noise removal using threshold Boolean filtering based on the impulse detection functions," *IEEE Signal Process. Lett.*, vol. 12, no. 1, pp. 63–66, Jan. 2005.
[5] P. S. Windyga, "Fast impulsive noise removal," *IEEE Trans. Image Process.*, vol. 10, no. 1, pp. 173–179, Jan. 2001.
[6] Z. Wang and D. Zhang, "Progressive switching median filter for the removal of impulse noise from highly corrupted images," *IEEE Trans. Circuits Syst. II*, vol. 46, no. 1, pp. 78–80, Jan. 1999.
[7] A. Diaz-Sanchez and J. Ramirez-Angulo, "An analog median filter with feedforward adaptation," in *Proc. 44th IEEE Midwest Symp. Circuit Syst.*, 2001, vol. 1, pp. 142–145.
[8] T. Alparone, S. Baronti, and R. Carla, "Two-dimensional rank-conditioned median filter," *IEEE Trans. Circuits Syst. II*, vol. 42, no. 2, pp. 130–132, Feb. 1995.
[9] G. Pok, J. C. Liu, and A. S. Nair, "Selective removal of impulsive noise based on homogeneity level information," *IEEE Trans. Image Process.*, vol. 12, no. 1, pp. 85–92, Jan. 2003.
[10] G. Garnett, T. Huegerich, C. Chui, and W. He, "A universal noise removal algorithm with an impulse detector," *IEEE Trans. Image Process.*, vol. 14, no. 11, pp. 1747–1754, Nov. 2005.
[11] K. D. Rao and G. Rajashekar, "Performance analysis of impulsive noisy image registration filters," in *Proc. INDICON*, Dec. 20–22, 2004, pp. 151–159.
[12] M. Saeed, H. R. Rabiee, W. C. Kar, and T. Q. Nguyen, "Bayesian Restoration of Noisy Images With the EM Algorithm," in *Proc. ICIP*, 1997, pp. 322–5.
[13] S. Ambike, J. Ilow, and D. Hatzniakos, Detection for binary transmission in a mixture of Gaussian noise and impulsive noise modeled as an alpha-stable process Dept. Electrical Eng., Univ. Toronto, Toronto, ON, Canada, Commun. Group Tech. Rep. 93-3, 1993 [Online]. Available: http://citeseer.ist.psu.edu/ambike93detection.html
[14] Y. C. Eldar and A. Yeredor, "Finite-Memory Denoising in Impulsive Noise Using Gaussian Mixture Models," *IEEE Trans. Circ. Syst. II Analog Digit. Signal Process.*, vol. 48, no. 11, pp. 1069–77, Nov. 2001.
[15] J. H. Miller and J. B. Thomas, "The detection of signals in impulsive noise modeled as a mixture process," *IEEE Trans. Commun.*, vol. 24, no. 5, pp. 560–3, May 1976.
[16] S. Webb, *The Physics of Medical Imaging*. Bristol, U.K.: Adam Hilger, 1988, pp. 29–32–571–576.
[17] M. M. Hadhoud, "X-rays images enhancement using human visual system model properties and adaptive filters," in *Proc. ICAASP*, May 2001, vol. 3, pp. 2005–2008.
[18] X. Huang, A. C. Madoc, and A. D. Cheethan, "Wavelet based bayesian estimator for Poisson noise removal from images," in *Proc. ICME*, Jul. 2003, vol. 1, no. 6–9, pp. 593–596.
[19] P. M. Goebel, A. N. Belbachir, and M. Truppe, "Noise estimation in panoramic x-rays images: An application analysis approach," in *Proc. 13th IEEE Workshop Statistical Signal Proc.*, 2005, pp. 996–1001.
[20] N. A. Weiss, *Introductory Statistics*, 6th ed. : Addison Wesley, 2002.
[21] M. J. Yaffe and J. A. Rowlands, "X-ray detectors for digital radiography," *Phys. Med. Biol.*, vol. 42, pp. 1–39, 1997.
[22] I. Csiszar, "Why least squares and maximum entropy? an axiomatic approach to inference for linear inverse problems," *Ann. Stat.*, vol. 19, pp. 2032–66, 1991.
[23] A. V. Oppenheim and R. W. Schafer, *Digital Signal Processing*. New York: Prentice Hall, Jan. 2, 1975.
[24] E. W. Weisstein, Stirling's approximation [Online]. Available: http://mathworld.wolfram.com/StirlingsApproximation.html
[25] J. A. Nelder and R. Mead, "Simplex method for function minimization," *Comput. J.*, vol. 7, pp. 308–313, 1965.
[26] W. H. Press, B. P. Flannery, S. A. Teukolsky, and W. T. Vetterling, *Numerical Recipies in C*. Cambridge, U.K.: Cambridge Univ. Press, 1992.
[27] K. Madsen, H. B. Nielsen, and O. Tingleff, Methods for non-linear least squares problems2nd ed. 2004 [Online]. Available: http://www2.imm.dtu.dk/courses/02611/nllsq.pdf, 2004
[28] T. Fawcett, ROC graphs: Notes and practical considerations for data mining researchers Palo Alto, CA, Tech. Rep. HPL-2003-4. HP Lab., 2003.

[29] X. D. Jang, "Image detail-preserving filter for impulsive noise attenuation," *IEE Proc.*, vol. 150, no. 3, pp. 179–185, Jun. 2003.
[30] I. Frosio and N. A. Borghese, "Offset and gain maps compression for digital radiographic sensors," in *Proc. CARS*, Osaka, Japan, Jun. 2006.
[31] V. Y. Panin, G. L. Zeng, and G. T. Gullberg, "Total variation regulated EM algorithm," *IEEE Trans. Nucl. Sci.*, vol. 46, no. 6, pp. 2202–10, Dec. 1999.
[32] S. Siltanen, V. Kolehmainen, S. Jarvenpaa, J. P. Kaipio, P. Koistinen, M. Lassas, J. Pirttila, and E. Somersalo, "Statistical inversion for medical x-ray tomography with few radiographs: I. General theory," *Phys. Med. Biol.*, vol. 48, pp. 1437–63, 2003.